Interference in $\omega - 2\omega$ atomic ionization within the strong-field approximation: Beyond the perturbative regime

Diego G. Arbó[1,2], Sebastián D. López[1],
[1] *Institute for Astronomy and Space Physics - IAFE (CONICET-UBA), CC 67, Suc. 28, C1428ZAA, Buenos Aires, Argentina. and*
[2] *Universidad de Buenos Aires, Facultad de Ciencias Exactas y Naturales y Ciclo Básico Común, Buenos Aires, Argentina.*
(Dated: December 12, 2021)

We analyze interference processes in atomic ionization induced by a two-color laser with fundamental frequency ω and its second harmonic 2ω. The interplay between inter- and intracycle interference processes give rise to multiphoton peaks which can be named as main or ATI peaks and sidebands, in analogy to the well-known RABBIT (reconstruction of attosecond harmonic beating by interference of two-photon transitions). We use the saddle point approximation (SPA) to extract the complex ionization times of the interfering electron trajectories. Changing the relative phase between the two colors, the doubly differential momentum distribution of emitted electrons can be controlled. We study the dependence of the electron emission as a function of the relative phase between the ω and 2ω fields within the strong field approximation (SFA) but beyond the perturbative regime. We focus on the extraction of the phase delays accounting the electron forward emission in the direction of the polarized electric fields. We characterize the time delays in the emission of electrons for visible frequency of the pump and its first harmonic as a probe [Ti:Sapphire laser (800 nm) together with the first harmonic (400 nm)] for a typical $\omega - 2\omega$ configuration for argon ionization. We find excellent agreement between our SPA results and the corresponding SFA (without any further approximation) and also with previous perturbative theories.

PACS numbers: 32.80.Rm,32.80.Fb,03.65.Sq

I. INTRODUCTION

Photoionization is defined as the detachment of one or multiple electrons from a system, such as an atomic or molecular ion, a cluster, or a solid, due to the electromagnetic force exerted by external radiation. Two different pictures has been widely used to depict the photoionization process. On one hand, the exiting electron tunnels through the barrier formed by the parent structure and the external field when the time that the electron travels through the barrier is longer than the time variation of the external field (situation known as the tunneling regime). And on the other hand, when the variation of the external field is very rapid, tunneling is not possible and photoionization proceeds through the absorption of one or several photons allowing the target gain energy up to the continuum near threshold or even higher (situation known as the multiphoton regime) [1–3]. First experiments used rather weak lasers, for which, the ionization processes were deep in the multiphoton regime [4]. Theories accompanying these experiments were firstly perturbative [5, 6] but, as irradiance of laser beams grew, these perturbation theories became obsolete and a new paradigm was necessary [7–9]. Based on rather simple pictures of the photoionization processes like the simpleman's model (SMM) or the strong field approximation (SFA), interference structures in photoelectron spectra have been identified as a diffraction pattern from a time grating composed of inter- and intracycle interferences [10–13]. Whereas the intercycle interferences give rise to multiphoton peaks, intracycle interferences lead to a modulation of the ATI spectrum offering information on the subcycle ionization dynamics [11, 14, 15].

Metrology of atomic processes became accessible through pump-probe techniques such as attosecond streaking [16–18] and RABBIT (reconstruction of attosecond harmonic beating by interference of two-photon transitions) [19–21]. These techniques involve lasers of at least two very different frequencies: Electrons are emitted due to the absorption of an XUV field and probed by a moderately intense field in the near-infrared region of the electromagnetic spectrum. In this way, it was possible to measure phase shifts compatible with attosecond delays for noble gas atoms [22–25]. For attosecond streaking, the oscillating probe field moves classically the electron previously freed by the pump field, producing gains and losses of its final kinetic energy [16, 26]. In RABBIT, ionization is given by two consecutive high harmonics fields of odd parity followed by absorption or emission of a photon with the fundamental frequency. By analyzing the interference between these two ionization paths, the intrinsic phase shifts in above threshold ionization (ATI) spectra could be extracted by means of second-order perturbative calculations [27] or by analyzing the asymptotic behavior of the scattered electron wave packet from numerically exact solutions of the time-dependent Schrödinger equation (TDSE) [28–34].

Strong-field ionization by laser fields with commensurate frequencies and well-defined relative phase permits the tune and control of the emission process [14, 15, 35–37]. ATI by laser pulses using the fundamental component and one of its harmonics were investigated [35, 37, 38] and applied for controlled ionization [39–41], dichroism [42, 43], orientation of molecules [44], and control of

interference fringes in the electron momentum distribution [14, 15]. The temporal shape of the two-color field is determined by the intensities of the two components and their relative phase. Coherent phase control refers to the manipulations of some physical processes through the relative phase [37]. The concept of phase shifts and time delays in RABBIT has been extended by Zipp *et al.* [45] for two-color ($\omega - 2\omega$) lasers with controlled relative phase. Very recently, we have theoretically explored the extraction of $\omega-2\omega$ phase delays by means of the *ab initio* solution of the TDSE and also through the development of a perturbation theory [46].

In this work, we developed a non-perturbation theory of the electronic photoemission process in atomic argon due to a two-color ($\omega - 2\omega$) linearly polarized short laser pulse in the multiphoton regime. In Sec. II, we introduce the general theory based on the saddle point approximation (SPA) to calculate the ionization time of each interfering electron trajectory, firstly analyzing one-color ionization and then the $\omega - 2\omega$ setup. Different interference structures of the doubly differential momentum distribution are analyzed. We focus on the extraction of the phase shifts using directional emission in the forward direction. We show that our SPA results are in excellent agreement with the results of the SFA (without any further approximation) and also the perturbation theories in the literature [46, 47]. We make our final remarks in Sec. III. Atomic units ($e = \hbar = m_e = 1$ a.u.) are used throughout unless stated otherwise.

II. NON-PERTURBATIVE STRONG-FIELD APPROXIMATION

In general, ionization of an atomic system by a linearly polarized laser pulse can be considered in the single-active-electron approximation. The TDSE then reads

$$i\frac{\partial}{\partial t}\left|\psi(t)\right\rangle = \left[H_0 + H_{\rm int}(t)\right]\left|\psi(t)\right\rangle, \tag{1}$$

where $H_0 = \vec{p}^2/2 + V(r)$ is the time-independent atomic Hamiltonian, whose first term corresponds to the electron kinetic energy and its second term to the electron-core Coulomb interaction. In Eq. (1), $H_{\rm int}(t)$ corresponds to the interaction hamiltonian between the atomic system and the external radiation field. Because of the presence of the external laser field, the electron initially bound in an atomic state $|\phi_i\rangle$ can either remain in the same state, be excited to another atomic bound state, or be emitted to a final continuum state $|\phi_f\rangle$ with final momentum $\vec{k}$ and energy $E = k^2/2$. In the latter case, we call the process photoionization and the transition amplitude within the time-dependent distorted wave theory in the prior form is expressed as [48, 49]

$$T_{\rm if} = -i\int_{-\infty}^{+\infty} dt\,\langle\chi_f^-(\vec{r},t)|H_{\rm int}(\vec{r},t)|\phi_i(\vec{r},t)\rangle, \tag{2}$$

where $\phi_i(\vec{r},t) = \varphi_i(\vec{r})\,e^{iI_p t}$ is the initial atomic state with ionization potential I_p and $\chi_f^-(\vec{r},t)$ is the distorted final state. Eq. (2) is exact as far as the final channel $\chi_f^-(\vec{r},t)$ is the exact solution of Eq. (1), within the dipole approximation. Throughout this paper, we will be considering linearly polarized laser fields (in the $\hat{z}$ direction).

Several degrees of approximation have been considered in the literature to solve Eq. (2). The widest known one is the strong field approximation (SFA), which neglects the Coulomb distortion (in the final channel) produced on the ejected-electron state due to its interaction with the residual ion and discard the influence of the laser field in the initial ground state and the depletion of the ground state [8, 50]. The SFA consists in approximating the distorted final state with the solution of the TDSE for a free electron in an electromagnetic field, namely, a Volkov function [51], i.e., $\chi_f^-(\vec{r},t) = \chi_f^V(\vec{r},t)$, where

$$\chi_f^V(\vec{r},t) = \frac{1}{(2\pi)^{3/2}}\exp\{i[\vec{k}+\vec{A}(t)]\cdot\vec{r}\} \times \exp\left\{\frac{i}{2}\int_t^\infty [\vec{k}+\vec{A}(t')]^2 dt'\right\} \tag{3}$$

the vector potential due to the total external field is defined as $\vec{A}(t) = -\int_{-\infty}^t dt'\vec{F}(t')$, and $\vec{F}(t)$ denotes the external laser field. The final Volkov function in Eq. (3) is calculated within the length gauge, i.e., $H_{\rm int}(\vec{r},t) = \vec{F}(t)\cdot\vec{r}$.

Therefore, T-matrix in Eq. (2) can be written as

$$T_{\rm if} = \int_{-\infty}^{+\infty} \ell(t)\; e^{iS(t)}\; dt, \tag{4}$$

where

$$\ell(t) = -i\vec{F}(t)\cdot\vec{d}\left[\vec{k}+\vec{A}(t)\right]$$

and

$$S(t) = -\int_t^\infty dt'\left\{\frac{\left[\vec{k}+\vec{A}(t')\right]^2}{2} + I_p\right\} \tag{5}$$

with the dipole transition moment defined as $\vec{d}(\vec{v}) = (2\pi)^{-3/2}\langle e^{i\vec{v}\cdot\vec{r}}|\vec{r}|\varphi_i(\vec{r})\rangle$, and $S(t)$ is the Volkov action.

We assume that the pump field is composed of $2N$ optical cycles each of duration $T = 2\pi/\omega$. Then,

$$\begin{aligned} T_{\rm if} &= \int_0^{NT} \ell(t)e^{iS(t)}\; dt \\ &= \sum_{j=0}^{N-1}\int_{jT}^{(j+1)T} \ell(t)e^{iS(t)}dt. \end{aligned} \tag{6}$$

We consider now a general electric field (and vector potential) with a smooth envelope with a central flat-top region where both $\vec{F}(t)$ and $\vec{A}(t)$ are oscillating with period T. From Eq. (5), it is straightforward to realize that

$S(t) - at$ is a time-oscillating function with the same period of the laser field and vector potential,

$$S(t + jT) = S(t) + ajT, \tag{7}$$

where

$$a = \frac{k^2}{2} + I_p + U_p, \tag{8}$$

and $U_p = \int_t^{t+T} dt' A(t')^2$. In light of the periodicity properties of the action in Eq. (7) and that $\ell(t + jT) = \ell(t)$, the transition matrix $T_{\rm if}$ in Eq. (4) can be written in terms of the contribution of the first fundamental cycle or unit cell [13, 52],

$$\begin{aligned} T_{\rm if} &= \sum_{j=0}^{N-1} \int_{jT}^{(j+1)T} \ell(t + jT) e^{iS(t+jT)} dt \\ &= \sum_{j=0}^{N-1} e^{iajT} \int_0^T \ell(t) e^{iS(t)} dt \\ &= \frac{\sin(aTN/2)}{\sin(aT/2)} e^{(iaT(2N-1)/2)} I(\vec{k}). \end{aligned} \tag{9}$$

From the absolute value of the transition matrix we can extract probabilistic information, like the doubly differential momentum distribution or the angle resolved photoelectron spectrum. Because of the azimuthal symmetry, the electron distribution can be expressed in terms of only two physical magnitudes, i.e., the final electron momentum parallel k_z and transversal k_ρ to the field polarization direction or, alternatively, the final kinetic energy E and the final polar emission angle θ:

$$|T_{\rm if}|^2 = \frac{dP}{2\pi k_\rho dk_\rho dk_z} = \frac{dP}{2\pi\sqrt{2E}\; dE\; d(\cos\theta)}. \tag{10}$$

The factor $I(\vec{k}) = \int_0^T \ell(t) e^{iS(t')} dt'$ in Eq. (9) corresponds to the contribution into one optical cycle of the ω field and $|I(\vec{k})|^2$ is known in the literature as the *intracycle* contribution to the ionization probability [49, 52, 53]. Thus, the photoelectron spectrum (PES) can be expressed as a product of the *intracycle* factor $|I(\vec{k})|^2$ and the *intercycle* factor $(\sin(aTN/2)/\sin(aT/2))^2$, being the latter the result of the phase interference arising from the N different optical cycles of the field [11–13]. We want to point out that Eq. (9) is a mere consequence of the periodicity of the transition matrix with no further approximations, except for a flat-top pulse [52].

Finite maxima are reached at the zeroes of the denominator of the intercycle factor $(\sin(aTN/2)/\sin(aT/2))^2$, i.e., the energy values satisfying $aT/2 = n\pi$, since the numerator also cancels out at these points. Such maxima are recognized as the multiphoton peaks of the PES. They occur when

$$E_n = n\omega - I_p - U_p, \tag{11}$$

where we have used Eq. (8). In fact, when $N \to \infty$, the intercycle factor becomes a series of delta functions, i.e., $\sum_n \delta(E - E_n)$, satisfying the conservation of energy. Instead, for finite pulse durations $\tau = NT$ (composed of N cycles), each multiphoton peak has a width $\Delta E \sim 2\pi/NT$, fulfilling the uncertainty relation $\Delta E\tau \sim 2\pi$.

The intracycle amplitude $I(\vec{k}) = \int_0^T \ell(t) e^{iS(t')} dt'$ in Eq. (9) can be calculated either numerically (SFA) or within the saddle point approximation (SPA). In the latter, the intracycle amplitude can be regarded as a superposition of all electron trajectories within any optical cycle or unit cell with final momentum $\vec{k}$

$$I(\vec{k}) \simeq \sum_\beta \ell(t_\beta) \frac{e^{iS(t_\beta)}}{\left|\ddot{S}(t_\beta)\right|^{1/2}}, \tag{12}$$

each starting at a complex ionization times t_β fulfilling the saddle equation $\dot{S}(t_\beta) = 0$ (where the dot denotes the time derivative), i.e.,

$$\frac{\left[\vec{k} + \vec{A}(t_\beta)\right]^2}{2} + I_p = 0. \tag{13}$$

In general, solutions of Eq. (13) come in pairs (t_β, t_β^*), where the star means complex conjugate. From each couple, we select only the solution with positive imaginary part to avoid spurious exponential growth of probabilities and only keep exponential decays when calculating $\exp[iS(t_\beta)] = \exp\{i\,\mathrm{Re}[S(t_\beta)]\} \exp\{-\mathrm{Im}[S(t_\beta)]\}$ in Eq. (12). The SMM considers real ionization times by neglecting I_p and the perpendicular momentum reducing Eq. (13) to $k_z + A(t_\beta) = 0$.

A. One color photoionization

For the case of atomic photoionization by a one color field $\vec{F}(t) = Ff(t)\cos(\omega t + \phi)\,\hat{z}$ with $f(t)$ a smooth function between 0 and 1 mimicking the pulse envelope, $\hat{z}$ the polarization direction, and F the field strength, the action can be calculated from Eq. (5) as

$$S_0(t) = at + b\cos(\omega t) + c\sin(2\omega t), \tag{14}$$

where a is given by Eq. (8), $b = F/\omega^2 \hat{z}\cdot\vec{k}$, $c = -U_p/2\omega$, and the ponderomotive energy is $U_p = (F/(2\omega))^2$. We denote S_0 the one-color action just to distinguish it from the two-color action in the next subsection.

From Eq. (13), two ionization times can be analytically calculated with the following expressions

$$\begin{aligned} t_1 &= \frac{1}{\omega}\sin^{-1}\left[\frac{\omega}{F}\left(k_z + i\sqrt{2I_p + k_\rho^2}\right)\right], \\ t_2 &= \frac{\pi}{\omega} - t_1^*, \end{aligned} \tag{15}$$

for $k_z \geq 0$ and,

$$\begin{aligned} t_1 &= \frac{\pi}{\omega} + \frac{1}{\omega}\sin^{-1}\left[\frac{\omega}{F}\left(k_z + i\sqrt{2I_p + k_\rho^2}\right)\right], \\ t_2 &= \frac{3\pi}{\omega} - t_1^*, \end{aligned} \tag{16}$$

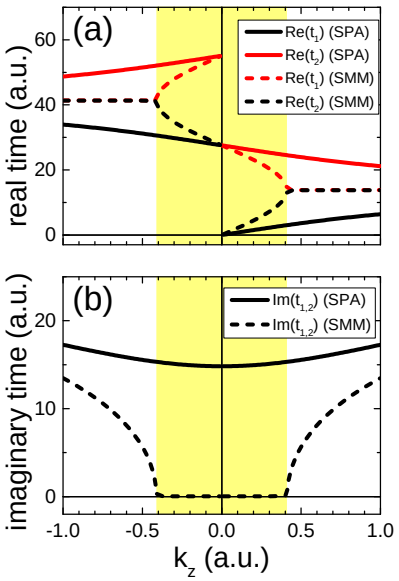

FIG. 1. Complex saddle times t_1 and t_2 as a function of the longitudinal momentum k_z for $k_\perp = 0$ for one-color ionization. In solid (dash) lines the results of the SPA (SMM, including an ionization potential of 10^{-6} to generate the imaginary part of the saddle time). (a) In black $\mathrm{Re}(t_1)$ and in red $\mathrm{Re}(t_2)$. (b) In solid (dash) lines the results of the SPA (SMM) $\mathrm{Im}(t_1) = \mathrm{Im}(t_2)$. The yellow region in the k_z domain corresponds to the allowed classical region in the SMM. In the classical-forbiden region, the imaginary part of the SMM saddle times increases.

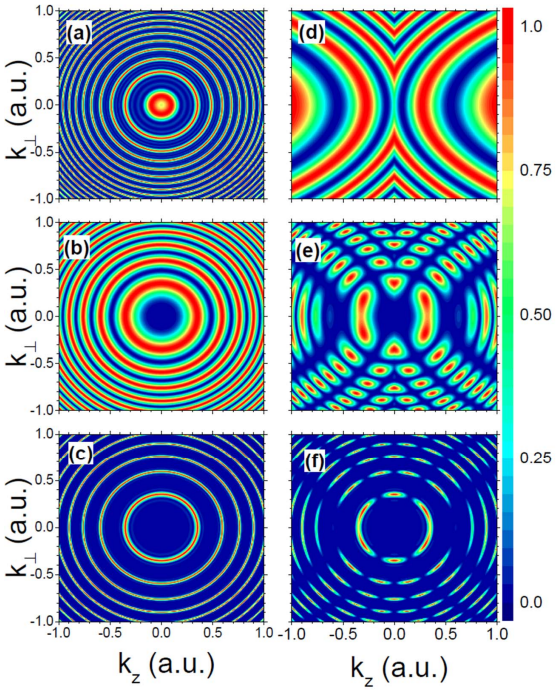

FIG. 2. Doubly differential momentum distribution as a function of the longitudinal momentum k_z and the perpendicular momentum $k_\perp$ for one-color (2ω) ionization. (a) Intercycle factor considering $4\pi/\omega$ periodicity generating ATI and SB rings, (b) Intercycle factor considering $2\pi/\omega$ periodicity generating only ATI rings (of double width), (c) Multiplication of (a) and (b), the ATI rings are visible but the SB rings disappeared since they coincide with the minima of the distribution in (b). (d) corresponds to the intracycle interference, (e) to the multiplication of distributions in (d) and (b), and in (f) the total momentum distribution is displayed (multiplication of (c) and (d)).

for $k_z \leq 0$.

We show the real part of t_1 and t_2 in Fig. 1a and the imaginary parts in Fig. 1b for an electric field of strength $F = 0.0469$ a.u. and frequency $\omega = 0.114$, for the special case that $k_\perp = 0$ (forward and backward emission). The SMM times are drawn in dash line and were calculated by including a tiny ionization potential $I_p = 10^{-6}$. The shaded region of longitudinal momentum $|k_z| \leq 2\sqrt{U_p}$ corresponds to the classical accessible region for the electron according to the SMM. Inside this region $\mathrm{Im}(t_1) = \mathrm{Im}(t_2) = 0$ while outside, $\mathrm{Im}(t_1) = \mathrm{Im}(t_2) > 0$. In turn, for the SPA, we have used an ionization potential $I_p = 0.58$ a.u. (corresponding to the ground state of atomic argon).

In Fig. 2a we show the intercycle factor $\left(\sin\left(aTN/2\right)/\sin\left(aT/2\right)\right)^2$ with $N = 4$ as a function of the longitudinal momentum k_z and the perpendicular momentum $k_\perp$ (whose magnitude is equal to k_ρ. Isotropic rings are observed at radii $k_n = \sqrt{2E_n}$, where E_n are given by Eq. (11), corresponding to the absorption of n photons. The intracycle factor is displayed in Fig. 2d exhibiting a strong angular dependence. The total doubly differential momentum distribution is proportional to the multiplication of the intercycle and intracycle factors and is displayed in Fig 2f. In this paper we omit in the calculations the factor $l(t)$ containing the atomic dipole moment just to focus on interference aspects of the photoionization processes.

B. Interference in $(\omega - 2\omega)$ photoionization

The main goal of this work is to extend the well-known interference structures of electron photoemission in one-color atomic photoionization to the case of two colors, where one main frequency (harmonic) doubles the other (fundamental), i.e., $\omega - 2\omega$ photoionization emission, within the SFA. If the fundamental intensity is very low compared to the intensity of its second harmonic, some connection between $\omega - 2\omega$ ionization and RABBIT can be speculated and analyzed showing some similarities and some differences [45–47]. In the RABBIT jargon for even n in Eq. (11), the energy maxima are named ATI peaks and for odd n they are named sidebands, but although in our context that denomination

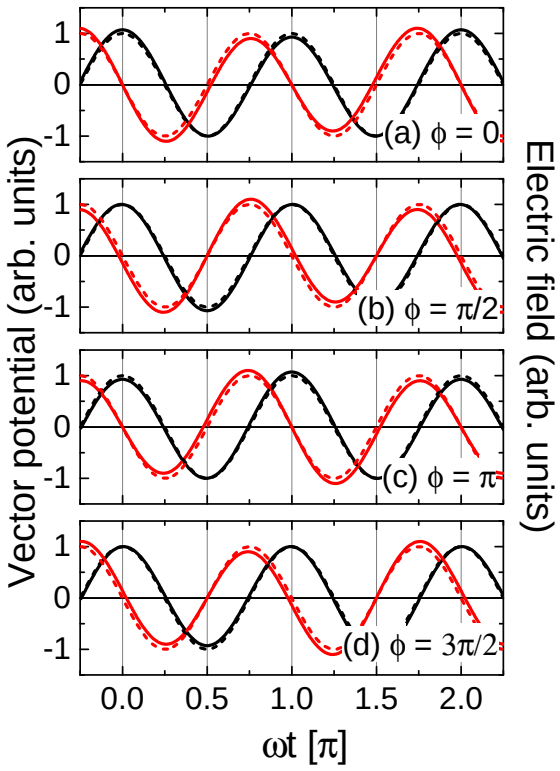

FIG. 3. Vector potential (red) and electric field (black) along the polarization axis as a function of time. In solid line the two-color version and in dash line the one-color version (switching off the ω terms in Eqs. (17) and (18). (a) for $\phi = 0$, (b) for $\phi = \pi/2$, (c) for $\phi = \pi$, and (d) for $\phi = 3\pi/2$. Vector potentials and electric fields are normalized with respect to their respective one-color version.

of the multiphoton peaks is arbitrary, we will maintain it for clarity. In general $n = n_{2\omega} + n_\omega$ denotes the absorption (emission) of a $n_{2\omega}$ number of 2ω photons and absorption (emission) and a n_ω number of ω photons for positive (negative) $n_{2\omega}$ and n_ω values. We consider the two-color electric field of the form

$$\vec{F}(t) = f(t)\left[F_{2\omega}\cos(2\omega t) + F_\omega \cos(\omega t + \phi)\right]\ \hat{z}, \quad (17)$$

with ϕ the relative phase of the second harmonic with respect to the fundamental laser field, $f(t)$ is a smooth function between 0 and 1 mimicking the pulse envelope, $\hat{z}$ is the polarization direction of both fields, and $F_{2\omega}$ and F_ω are the field strengths of the second harmonic and fundamental frequency, respectively. For a long pulse with adiabatic switch on and off the vector potential can be written in its central part $f(t) \simeq 1$), as

$$\vec{A}(t) = -f(t)\left[\frac{F_{2\omega}}{2\omega}\sin(2\omega t) + \frac{F_\omega}{\omega}\sin(\omega t + \phi)\right]\hat{z}, \quad (18)$$

giving rise to a periodicity property of the vector potential and the electric field, i.e., $\vec{A}(t) = \vec{A}(t + 2j\pi/\omega)$ and $\vec{F}(t) = \vec{F}(t + 2j\pi/\omega)$, with j any integer number provided that $f(t + 2j\pi/\omega) = 1$. For our calculations we use the same parameters as in Ref. [45] with $F_{2\omega} = 0.0469$ a.u. ($I_{2\omega} = 8 \times 10^{13}$ W/cm^2) and $F_\omega = 0.00332$ a.u. ($I_\omega = 4 \times 10^{11}$ W/cm^2). In Fig. 3 we show the electric field in black and the vector potential in red as a function of time. We have normalized both fields to the one-color case ($F_\omega = 0$) displayed in dotted lines. As the one-color fields show obviously invariant under changes of the relative phase, there are small but appreciable changes in the two-color fields. For example, the one-color fields are π/ω-periodic, whereas the two-color fields are $2\pi/\omega$-periodic. As shown for the one-color case [11, 12], the correct way to choose the unit cell corresponding to one optical cycle of the field is from a root of the vector potential. For the one-color case this corresponds to, for example, $t = 0$, whereas this value changes for the two-color case as a function of the relative phase ϕ. For example, considering the roots of the vector potential closest to the origin as the left border of the unit cells, they are determined by $t \in [0, 2\pi/\omega]$ ($\phi = 0$ in Fig. 3a), $t \in [-1.243, -1.243 + 2\pi/\omega]$ (in a.u. for $\phi = \pi/2$ in Fig 3b), $t \in [0, 2\pi/\omega]$ ($\phi = \pi$ in Fig. 3c), and $t \in [1.243, 1.243 + 2\pi/\omega]$ (in a.u. for $\phi = 3/2$ in Fig. 3d).

Under the assumption of adiabatic switch on and off, the action in Eq. (5) can be analytically calculated (in the central region where $f(t) = 1$) as

$$\begin{aligned} S(t) = {} & at + b\cos(2\omega t) + c\sin(4\omega t) + d\cos(\omega t + \phi) \quad (19) \\ & + e\sin(\omega t - \phi) + f\sin(2\omega t + 2\phi) + g\sin(3\omega t + \phi), \end{aligned}$$

where a is given by Eq. (8), and

$$\begin{aligned} b &= \frac{F_{2\omega}}{4\omega^2}\hat{z}\cdot\vec{k}, \quad (20) \\ c &= -\frac{U_{p,2}}{4\omega}, \\ d &= \frac{F_\omega}{\omega^2}\hat{z}\cdot\vec{k}, \\ e &= \frac{F_{2\omega}F_\omega}{4\omega^3}, \\ f &= -\frac{U_{p,1}}{2\omega}, \\ g &= -\frac{F_{2\omega}F_\omega}{12\omega^3}, \end{aligned}$$

and $U_p = U_{p,2} + U_{p,1} = (F_{2\omega}/(4\omega))^2 + (F_\omega/(2\omega))^2$ defines the ponderomotive energy as the addition of the individual ponderomotive energies of each color. We we have dropped diverging terms in Eq. (19) since only the accumulated action, computed as differences of phases, is relevant. The two-color action of Eq. (19) reduces to the one-color action of Eq. (14) when either $F_\omega = 0$ (since $d = e = f = g = 0$) or $F_{2\omega} = 0$ (since $b = c = e = 0$).

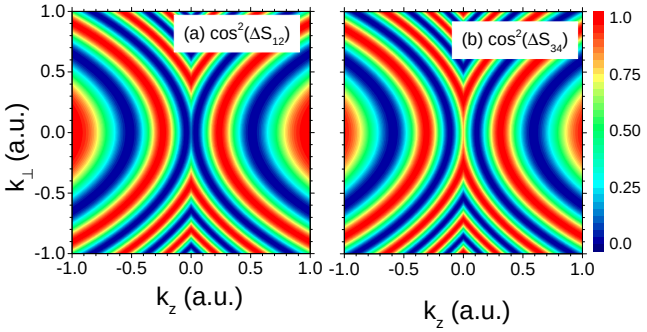

FIG. 4. Intrahalfcycle factors $\cos^2(\Delta S_{12}/2)$ in (a) and $\cos^2(\Delta S_{34}/2)$ in (b).

For the case of an $\omega - 2\omega$ field with weak probe ω field compared to the harmonic 2ω field, there are four physical solutions of Eq. (13) per optical cycle (in the unit cell), i.e., t_1, t_2, t_3, and t_4. We have solved all the saddle times from Eq. (13) numerically by separating their real and imaginary parts obtaining two coupled equations:

$$\frac{F_{2\omega}}{2\omega}\sin(2\omega\,\mathrm{Re}\,t_\beta)\cosh(2\omega\,\mathrm{Im}\,t_\beta) + \frac{F_\omega}{\omega}\sin(\omega\,\mathrm{Re}\,t_\beta+\phi)\cosh(\omega\,\mathrm{Im}\,t_\beta) = k_z \quad (21)$$

$$\frac{F_{2\omega}}{2\omega}\cos(2\omega\,\mathrm{Re}\,t_\beta)\sinh(2\omega\,\mathrm{Im}\,t_\beta) + \frac{F_\omega}{\omega}\cos(\omega\,\mathrm{Re}\,t_\beta+\phi)\sinh(\omega\,\mathrm{Im}\,t_\beta) = i\sqrt{2I_p+k_\rho^2}, \quad (22)$$

with $\beta = 1, 2, 3$, and 4. By neglecting either the first or the second terms of Eq. (22) and summing the two equations we recover the saddle times in Eqs. (16) and (15) for the one-color case.

From Eq. (12), the intracycle amplitude stemming from the electron trajectories with released times t_β ($\beta = 1, 2, 3$, and 4) is proportional to

$$\sum_{\beta=1}^{4} e^{iS(t_\beta)} = e^{i\overline{S}_{1,2}}\cos\left[\frac{\Delta S_{1,2}}{2}\right] + e^{i\overline{S}_{3,4}}\cos\left[\frac{\Delta S_{3,4}}{2}\right] \quad (23)$$

where we have omitted the prefactors of each of the terms corresponding to the electron trajectories departing at t_1, t_2, t_3, and t_4, to highlight the interference patterns. In Eq. (23) $\overline{S}_{i,j} = [S(t_i) + S(t_j)]/2$ is the average action between t_i and t_j and $\Delta S_{i,j} = S(t_j) - S(t_i)$ is the accumulated action between t_i and t_j. The accumulated actions $\Delta S_{1,2}$ and $\Delta S_{3,4}$ in the last equation contribute to the intrahalfcycle interference of the first and second half cycles. In Fig. 4 we compare the intrahalfcycle factors of the first and second half cycles. They are similar but not equal since the vector potential in the first half cycle differs from the second half cycle. As the probe field is weak compared to the pump field, the intrahalfcycle distributions of Fig. 4 are also similar to the one color case exhibited in Fig. 2d. Taking the zeroth-order perturbation in the probe field $(\Delta S_0)_{1,2} = (\Delta S_0)_{3,4} \equiv \Delta S_0$, where ΔS_0 denotes the one-color accumulated action in Eq. (14) . Therefore, the probability,calculated as the square of the absolute value of the coherent addition of the four different terms in Eq. (23), can be written as

$$\left|\sum_{\beta=1}^{4} e^{iS(t_\beta)}\right|^2 \simeq \left|e^{i\overline{S}_{1,2}} + e^{i\overline{S}_{3,4}}\right|^2 \cos^2\left[\frac{\Delta S_0}{2}\right] \simeq 4\underbrace{\cos^2\left(\frac{\Delta S}{2}\right)}_{\text{interhalfcycle}}\underbrace{\cos^2\left[\frac{\Delta S_0}{2}\right]}_{\text{intrahalfcycle}}, \quad (24)$$

where $\Delta S = \overline{S}_{3,4} - \overline{S}_{1,2}$. To get Eq. (24) we have considered the periodicity of $S_0(t)$. Eq. (24) shows that the intracycle factor $\left|I(\vec{k})\right|^2$ can be approximately splitted as two factors: (i) the intrahalfcycle interference pattern $\cos^2[\Delta S_0/2]$ stemming from the interference of the two electron trajectories released during half optical cycle of the ω field (or within one optical cycle of the 2ω field) and (ii) the interhalfcycle interference between the contribution of the two half cycles of the ω field (or between the two optical cycle of the 2ω field).

If we go back to one-color ionization, i.e., $S(t) = S_0(t)$, which fulfills the periodicity property $S_0(t + jT/2) = S_0(t) + ajT/2$. Then, $\overline{S}_{3,4} = \overline{S}_{1,2} + aT/2$, and $\Delta S = \Delta S_0 = aT/2 = a\pi/\omega = (E + I_p + U_p)\pi/\omega$. Replacing the energy for its value at the multiphoton peaks in Eq. (11), then $\Delta S_0 = n\pi$. Therefore, the intracycle factor $\cos(\Delta S_0/2)$ in Eq. (24) becomes equal to ± 1 for even n (constructive interference for the ATI peaks) and 0 for odd n (destructive interference for the sidebands). It can be observed that the odd intercycle rings in Fig 2a coincide with the minima of the intracycle factor in Fig. 2b. Thus, the sidebands are not formed in Fig. 2c and Fig. 2f, which simply means that sidebands are only present when an ω field is applied.

More generally and beyond the last approximation, complex ionization (saddle) times depend on the longitudinal and transverse momenta, similar to the one color case. For $\omega - 2\omega$ ionization, Fig. 5 displays the real parts of the saddle times t_1 (in black), t_2 (in green), t_3 (in cyan) and t_4 (in yellow) as a function of the longitudinal momentum k_z for $k_\perp = 0$ and for relative phases $\phi = 0, \pi/2, \pi$, and $3\pi/2$. The same is displayed for the imaginary parts of the ionization times. For each value of k_z, the different solutions of Eqs. (22) are very similar and cannot be distinguished in the figure. In Figs. 6 we show that the apparent degeneracy with respect of the relative phase is not such (close up of Fig. 4). Whereas for $k_z \geq 0$, $\mathrm{Re}(t_1)$ are the same for $\phi = 0$ and π and is zero for $k_z = 0$, it has smaller values for $\phi = \pi/2$ and higher values for $\phi = 3\pi/2$ being the difference of about

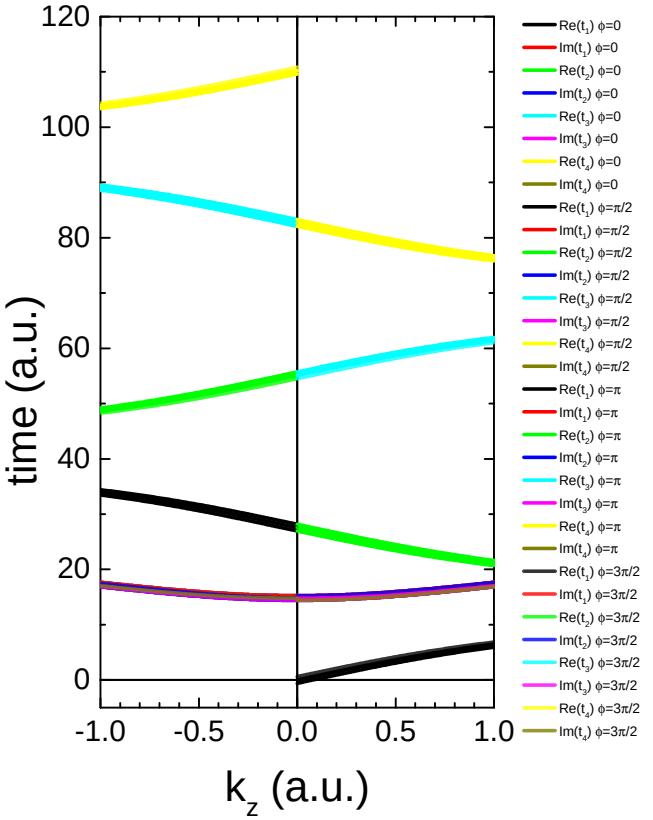

FIG. 5. Complex saddle times t_1, t_2, t_3, and t_4 as a function of the longitudinal momentum k_z for $k_\perp = 0$ for $\omega - 2\omega$ ionization. In solid (dash) lines the results of the SPA real (imaginary) parts for different relative phases $\phi = 0$, $\phi = \pi/2$, $\phi = \pi$, and $\phi = 3\pi/2$. The variation of both real and imaginary parts of the saddle times with the relative phase is very small and cannot be discerned in this figure.

1 a.u.. The degeneracy of $\mathrm{Re}(t_1)$ between $\phi = 0$ and π is removed for $k_z < 0$ at expenses of a new degeneracy between $\phi = \pi/2$ and $3\pi/2$. In Fig 7b, we show that $\mathrm{Re}(t_2)$ lying in the second quarter cycle are the same for $\phi = \pi/2$ and $3\pi/2$ for $k_z \geq 0$ whereas it has smaller values for $\phi = \pi$ and higher values for $\phi = 0$. The degeneracy of $\mathrm{Re}(t_2)$ between $\phi = \pi/2$ and $3\pi/2$ is removed for $k_z < 0$ at expenses of a new degeneracy between $\phi = 0$ and π. $\mathrm{Re}(t_3)$ lying in the third quarter cycle is shown in Figs. 6c. The degeneracy is the same as for $\mathrm{Re}(t_1)$ whereas it has smaller values for $\phi = 3\pi/2$ and higher values for $\phi = \pi/2$ for $k_z \geq 0$ and the inverse for $k_z < 0$. Finally, the same is observed for $\mathrm{Re}(t_4)$ with respect to $\mathrm{Re}(t_2)$ in Figs. 6d. We do not analyze the imaginary part of the ionization times in detail since it is not relevant for the interference patterns.

In Figs. 7 we show the SPA doubly differential pho-

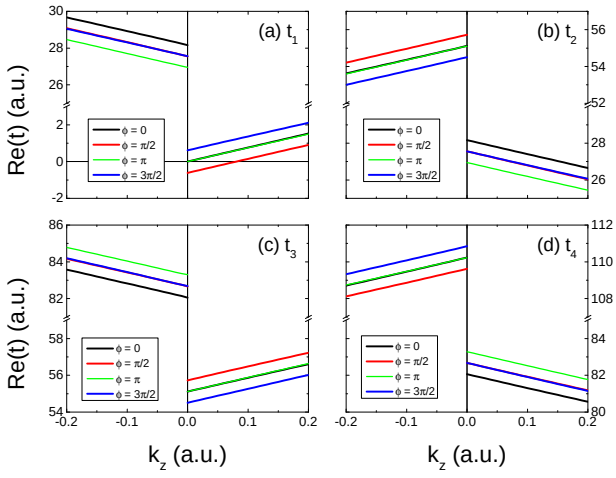

FIG. 6. Close up of the real parts of the saddle times of Fig. 4 for different relative phases (a) $\phi = 0$, (b) $\phi = \pi/2$, (c) $\phi = \pi$, and (d) $\phi = 3\pi/2$.

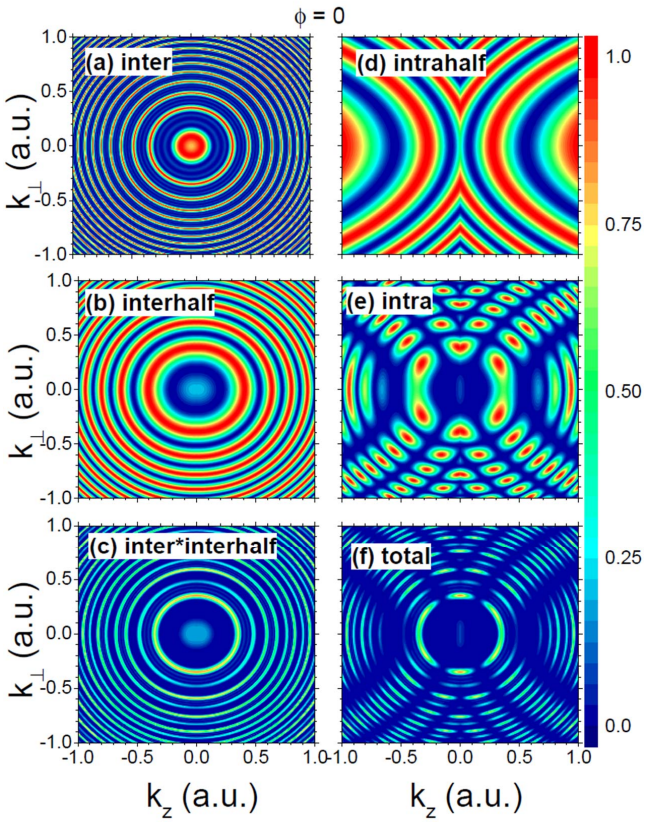

FIG. 7. Doubly differential momentum distribution as a function of the longitudinal k_z and perpendicular momenta $k_\perp$ for the $\omega - 2\omega$ ionization within the SPA with relative phase $\phi = 0$. (a) Intercycle factor, (b) interhalfcycle factor, (c) multiplication of (a) and (b), (d) intrahalfcycle factor, (e) intracycle factor [multiplication of distributions in (d) and (b)], and (f) the total momentum distribution [multiplication of (c) and (d)]. All distributions are normalized.

toelectron momentum distribution as a function of the longitudinal momentum k_z and the perpendicular momentum $k_\perp$ for zero relative phase ($\phi = 0$) between the two colors. The intercycle interference pattern for $N = 4$ displays in Figs. 7a a set of multiphoton (ATI and sidebands) peaks. The number of minima between consecutive multiphoton rings is $N-1 = 3$. This factor is practically the same as the one-color intercycle factor in Fig. 2a with an almost imperceptible difference stemming from the inclusion of the ponderomotive energy of the ω field, which is $U_{p,1} = 8.5 \times 10^{-4}$ (2% of $U_{p,2}$). The intercycle factor is also independent of the electron emission angle and the relative phase ϕ. The interhalfycle factor in Figs. 7b also consists in a set of concentric rings, but the isotropy is lost and the rings appear slightly stretched along the longitudinal momentum. Therefore, the minima of the intracycle rings do not perfectly match with the sidebands of the intercycle factor in Figs. 7a and thus, they survive when one multiply the inter- and intracycle factors as shown in Figs. 7c, unlike the one-color case. In Figs. 7d we show the intrahalfcycle factor calculated as the intrahalfcycle of the one color case, i.e., $\cos^2\left[(\Delta S_0)/2\right]$. Therefore, the intrahalfcycle pattern is independent of the relative phase ϕ. The intracycle pattern (multiplication of the interhalf- and intrahalfcycle patterns) is shown in Figs. 7e. The quasi-isotropic intracycle factor appears modulated by the highly angle-dependent intrahalfcycle pattern (or viceversa). The total emission pattern is the multiplication of the inter- (Figs. 7a) and intracycle (Figs. 7d) (see Fig. 7f). ATI peaks and sidebands of Figs. 7c modulated by the intracycle interference pattern are observed in Figs. 7d.

The doubly differential photoelectron momentum distribution as a function of the longitudinal momentum k_z and the perpendicular momentum $k_\perp$ for relative phase $\phi = \pi/2$ is shown in Figs. 8. The interhalfcycle factor in Figs. 8a also consists in a set of concentric rings with a discontinuity for $k_z = 0$ since the the vector potential is not antisymmetric (with respect to the middle of the unit cell) as in the case of $\phi = 0$ (see Fig. 3b). Such discontinuities are an artifact of the SPA and also appears for laser assisted photoionization emission (two colors with one frequency much higher than the other) [54, 55]. Again, the minima of the interhalfcycle rings do not match with the sidebands of the intercycle factor in Figs. 7a and thus, they survive when one multiply the inter- and interhalfcycle factors (see Fig. 8b). The intracycle factor in Fig 8c inherits the discontinuity of the interhalfcycle factor of Figs. 8a**.** The total emission pattern is the multiplication of the inter- (Figs. 7a) and intracycle (Figs. 8c) patterns (see Fig. 8d).

Despite the case of $\phi = \pi/2$, for $\phi = \pi$ the two half cycles have the same duration and the interhalfcycle distribution is continuous as displayed in Figs. 9a (as for $\phi = 0$). The multiplication of the intercycle factor of Figs. 7a and the interhalfcycle factor of Figs. 9a is displayed in Figs. 9b exhibiting all ATIs and sidebands. In Figs. 9c the intracycle pattern is displayed. The total

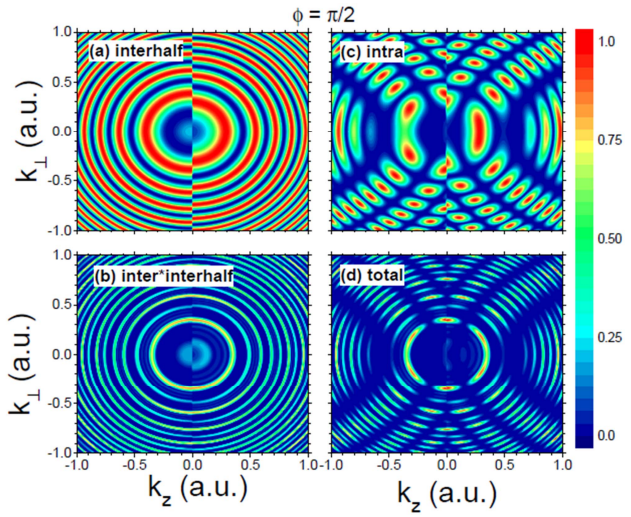

FIG. 8. Doubly differential momentum distribution as a function of the longitudinal momentum k_z and the perpendicular momentum $k_\perp$ for the $\omega - 2\omega$ ionization within the SPA with relative phase $\phi = \pi/2$. (a) interhalfcycle factor, (b) multiplication of the intercycle factor in Fig 7a and the interhalfcycle factor in Figs. 8a, (c) intracycle factor (multiplication of the intrahalfcycle factor in Figs. 7d and the interhalfcycle of Figs. 8a), and (d) total distribution calculated as the multiplication of the intercycle factor in Figs. 7a and the intracycle factor in Figs. 8c. All distributions are normalized.

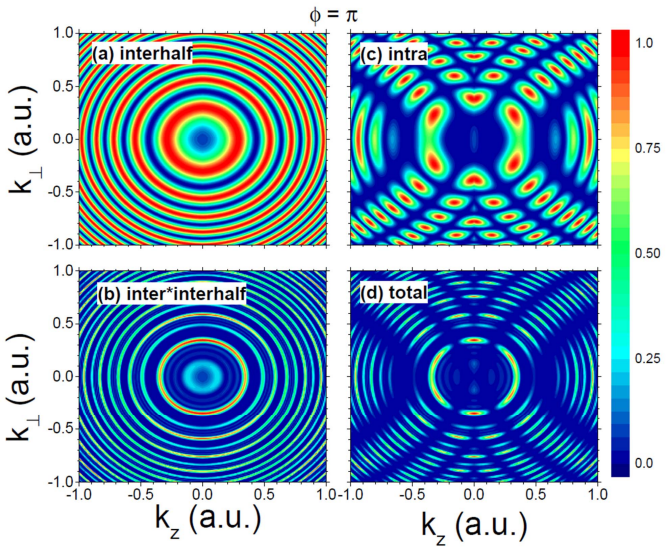

FIG. 9. Doubly differential momentum distribution as a function of the longitudinal momentum k_z and the perpendicular momentum $k_\perp$ for the $\omega - 2\omega$ ionization within the SPA with relative phase $\phi = \pi$.(a) interhalfcycle factor, (b) multiplication of the intercycle factor in Fig 7a and the interhalfcycle factor in Figs. 9a, (c) intracycle factor (multiplication of the intrahalfcycle factor in Figs. 7d and the interhalfcycle of Figs. 9a), and (d) total distribution calculated as the multiplication of the intercycle factor in Figs. 7a and the intracycle factor in Figs. 9c. All distributions are normalized.

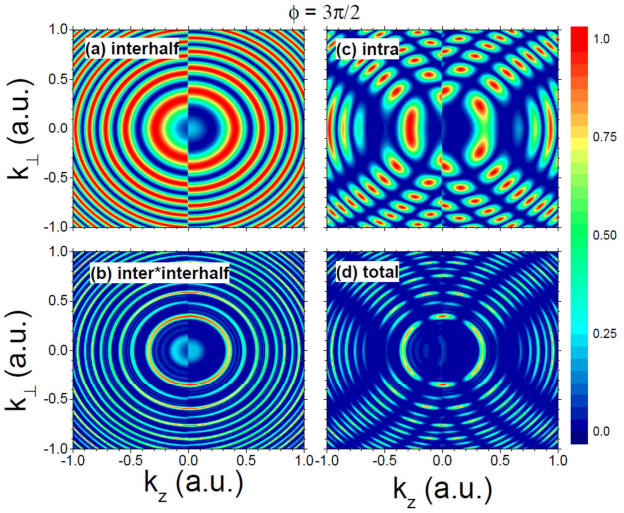

FIG. 10. Doubly differential momentum distribution as a function of the longitudinal momentum k_z and the perpendicular momentum $k_\perp$ for the $\omega - 2\omega$ ionization within the SPA with relative phase $\phi = 3\pi/2$. (a) interhalfcycle factor, (b) multiplication of the intercycle factor in Fig 7a and the interhalfcycle factor in Fig. 10a, (c) intracycle factor (multiplication of the intrahalfcycle factor in Figs. 7d and the interhalfcycle of Fig. 10a), and (d) total distribution calculated as the multiplication of the intercycle factor in Figs. 7a and the intracycle factor in Fig. 10c. All distributions are normalized.

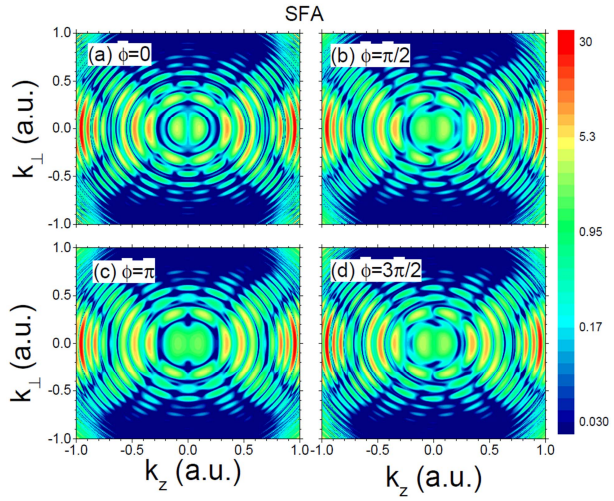

FIG. 11. Doubly differential momentum distribution as a function of the longitudinal momentum k_z and the perpendicular momentum $k_\perp$ for the $\omega - 2\omega$ ionization within the SFA with relative phase $\phi = 0$ in (a), $\phi = \pi/2$ in (b), $\phi = \pi$ in (c), and $\phi = 3\pi/2$ in (d). In order to highlight the interference patterns we have multiplied the momentum distribution by $\exp(10E)$ and plotted in logarithmic scale.

momentum distribution for $\phi = \pi$ is shown in Figs. 9d. For $\phi = 3\pi/2$ the first half cycle of the vector potential is shorter than its second half cycle, thus, bigger intracycle rings yield for positive k_z, as shown in Fig. 10a, instead of for negative k_z in the case for $\phi = \pi/2$. The multiplication of the intercycle factor of Figs. 7a and the interhalfcycle factor of Figs. 10a is displayed in Fig. 10b, which shows ATIs and sidebands. In Fig. 10c the intracycle interference pattern exhibits again a discontinuity like the case of $\phi = \pi/2$ in Figs. 8c. The total momentum distribution for $\phi = 3\pi/2$ is shown in Fig. 10d.

In order to test the validity of the SPA, we perform the time integral in Eq. (4) numerically within the SFA [49, 56, 57]. For the sake of simplicity, we model the atomic argon as a hydrogen-like atom with effective charge $Z_{\text{eff}} = \sqrt{2n^2 I_P}$, where n is the principal quantum number of the initial state, in this case $n = 3$ and the initial orbital quantum number is $l = 1$ (p-state) [58]. This effective charge ensures the ionization potential to be taken into account properly and, consequently, the intercycle fringes in the electron spectra to be situated at the energy values of Eq. (11). We consider an electric field with a ramp on and ramp off of duration $2\pi/\omega$ each and a flat-top region of duration $4\pi/\omega$. In Fig. 12 we show the doubly differential momentum distribution for relative phase $\phi = 0$ in (a), $\phi = \pi/2$ in (b), $\phi = \pi$ in (c), and $\phi = 3\pi/2$ in (d). In order to highlight the interference patterns we have multiplied the momentum distribution by $\exp(10E)$ and plotted in logarithmic scale to neutralize the exponential decay of the SFA as a function of the energy. The intercycle interference pattern appeared as concentric rings situated at $\sqrt{2E_n}$, whereas the intracycle interference pattern does it with the shape of waning and waxing moons (depending on the sign of k_z). Whereas distributions for $\phi = 0$ and π in Figs 12a and 12c exhibit forward-backward symmetry, the momentum distribution for $\phi = \pi/2$ results in a small asymmetry enhancing forward emission and, contrary, the momentum distribution for $\phi = 3\pi/2$ results in a small asymmetry enhancing backward emission. The agreement between the SPA distributions in Figs. 8f, 9f, 10f, and 11f and the SFA distributions in Figs. 11 is very good. Some differences for the angular distribution near threshold stem from the effect of the dipole matrix element (from a p-state to the continuum) in the SFA, which has been disregarded within the SPA. We have checked this performing calculations for a hydrogenic atom from a fictitious $1s$ state with $I_p = 0.58$ (not shown).

C. Phase delays in $\omega - 2\omega$ ionization

In order to get a simple close form, and considering that ionization takes place at times near the extremes of the electric field [Eq. (17)], at zeroth-order perturbation, these ionization times are $t_j = (j-1)\pi/(2\omega)$ with $j = 1, 2, 3,$ and 4. After a bit of algebra the accumulated action becomes

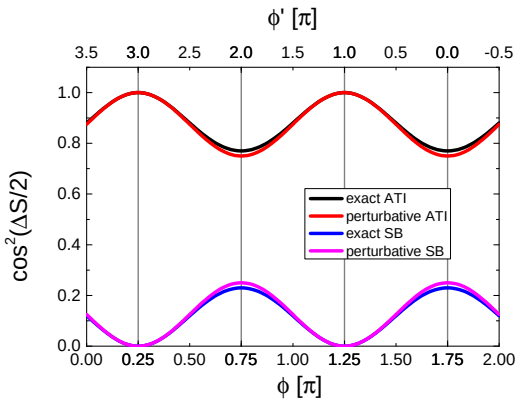

FIG. 12. SPA intracycle interference for ATI peaks and sidebands and their respective perturbative prediction both given by Eqs. (26) and (27) as a function of relative phases ϕ (lower axis) and ϕ' (upper axis) for $\chi = 0.5$. ATI maximizes at $\phi = 0.25\pi$ and 1.25π ($\phi' = 3\pi$ and π), whereas sidebands maximizes at $\phi = 0.75\pi$ and 1.75π ($\phi' = 2\pi$ and 0)

$$\begin{aligned}\Delta S &= n\pi + (-d - e + g)(\cos\phi - \sin\phi) \\ &= n\pi + 2\chi\cos(\phi + \pi/4),\end{aligned} \tag{25}$$

where $\chi = (-d - e + g)/\sqrt{2} = -F_\omega\left(k_z/\omega^2 + F_{2\omega}/(3\omega^3)\right)/\sqrt{2}$.

For an ATI peak, n is even then replacing Eq. (25) into Eq. (24) we demonstrate that the intracycle interference probability factor $\cos^2\left(\frac{\Delta S}{2}\right)$ is equal to

$$\cos^2[\chi\cos(\phi + \pi/4)] \simeq 1 - \frac{\chi^2}{2} + \frac{\chi^2}{2}\cos[2(\phi + 3\pi/4)] + O(\chi^4), \tag{26}$$

where in the last term we have performed a series expansion in terms of the perturbation parameter χ. This shows that the phase delay of an ATI peak is $\phi_0 = -3\pi/4$. In Fig. 12 we display the analytical expression $\cos^2[\chi\cos(\phi + \pi/4)]$ and its first order perturbative approximation $1 - \chi^2/2 + \chi^2\cos[2(\phi + 3\pi/4)]/2$ for the value $\chi = 0.5$ which reproduces the SFA value in [45] and the perturbative theory in [46].

Instead, for any sideband, n is odd and thus the intracycle interference probability factor $\cos^2\left(\frac{\Delta S}{2}\right)$ can be written as

$$\sin^2[\chi\cos(\phi + \pi/4)] \simeq \frac{\chi^2}{2} + \frac{\chi^2}{2}\cos[2(\phi + \pi/4)] + O(\chi^4), \tag{27}$$

where in the last term we have performed a series expansion in terms of the peturbation parameter χ. This shows that the phase delay of any sideband is $\phi_0 = -\pi/4$, or equivalently $\phi_0' = -2(\phi_0 + \pi/4) = 0$. In Fig. 12 we display the analytical expression $\sin^2[\chi\cos(\phi + \pi/4)]$ and its first order perturbative approximation $1 + \chi^2\cos[2(\phi + \pi/4)]/2$ for the value $\chi = 0.5$ which reproduces the SFA in [45] and the perturbative theory in [46]. The variation of the probabilities of the ATI peaks and sidebands as a function of the relative phase ϕ is small if χ is small, or equivalently, if the probe field is weak. It is worth to notice from Eqs. (26) and (27) that the probability of ATI peaks and sidebands as a function of the relative phase ϕ have opposite phases (phase difference of π), as expected. The fact that the addition of the intracycle pattern of ATI and sidebands is unity assures the conservation of probability. We obtain similar results to the non-perturbative theory in Ref. [34] for RABBIT. Especially, Eqs. (26) and (27) are similar to Eqs. (14) and (15) in [34]. The factor $\chi \simeq -\alpha k_z\left(1 + F_{2\omega}/(3\omega k_z)\right)/\sqrt{2} = -\vec{\alpha}_\omega\cdot\vec{k}\left(1 + \vec{\alpha}_{2\omega}\cdot\vec{k}/(3E_z)\right)/\sqrt{2}$, where $\vec{\alpha}_\omega = \vec{F}_\omega/\omega^2$, $\vec{\alpha}_{2\omega} = \vec{F}_{2\omega}/(2\omega)^2$ represents the quiver vector for the two different ω and 2ω fields and $E_z = k_z^2/2$. Therefore, it may be thought that the interhalfcycle interference pattern stem from two point sources

$$\cos^2[\chi\cos(\phi + \pi/4)] = \cos^2\left[\vec{k}\cdot\left(\vec{R}_+ - \vec{R}_-\right)/2\right] \quad \text{(ATI)} \tag{28}$$

$$\sin^2[\chi\cos(\phi + \pi/4)] = \sin^2\left[\vec{k}\cdot\left(\vec{R}_+ - \vec{R}_-\right)/2\right] \quad \text{(SB)}$$

at $\vec{R}_{+(-)} = \pm\vec{\alpha}_\omega\left(1 + \vec{\alpha}_{2\omega}\cdot\vec{k}/(3E_z)\right)\cos(\phi + \pi/4)/\sqrt{2}\hat{z}$, similar to a diatomic molecule aligned along the polarization axis. For the case of the ATIs, these two point sources emit in phase and constructuve interference is produced at perpendicular emission; instead, for sidebands, the two point sources emit in counterphase, leading to partial destructive interference in the perpendicular direction since in this case $\chi = -F_\omega F_{2\omega}/(3\sqrt{2}\omega^3)$ and not zero as for the emission from a diatomic molecule. In Figs. 7c, 8c, 9c, and 10c we observe a minimum as a function of the angle, whereas ATIs exhibit maxima values.

In Fig. 13 we show the energy spectrum in the forward direction as a function of the relative phase ϕ between the two colors within the SPA. In Fig 13a, we show that the intercycle factor is independent ϕ. All multiphoton peaks (ATIs and sidebands) are present in the intercycle factor in Fig. 13a with separation of one ω photon energy. The interhalfcycle factor can be observed as a 2π-periodic function in Fig. 12b. The separation between interhalfcycle maxima corresponds to a 2ω photon energy and the amplitude of the oscillation increases with energy, since the accumulated action ΔS in Eq. (25) increases with $k_z = \sqrt{2E}$ through the factor χ. The interplay between the inter- and interhalfcycle interferences is plotted in Fig. 13c where both ATI peaks and sidebands arise. From Eq. (11), we see that the first multiphoton peak just above threshold ($E_n = 0.0038$ a.u.) corresponds to $n = 11$ and, as it is an odd number, it is a sideband with $\phi_0 = 3\pi/4$ and $7\pi/4$ (as all sidebands). In turn, ATI peaks maximize at $\phi_0 = \pi/4$ and $5\pi/4$. This confirms our prediction of Eqs. (26) and (27) shown in Fig. 12.

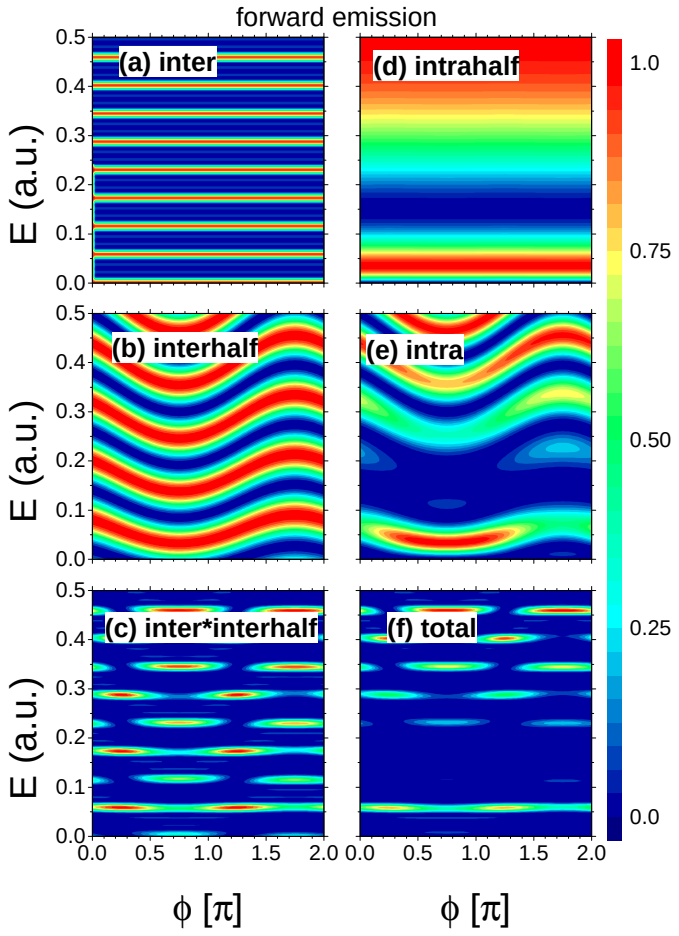

FIG. 13. Energy distribution in the forward direction as a function of the relative phase ϕ for the $\omega - 2\omega$ ionization within the SPA. (a) Intercycle factor, (b) interhalfcycle factor, (c) multiplication of (a) and (b), (d) intrahalfcycle factor, (e) intracycle factor [multiplication of distributions in (b) and (d)], and (f) the total momentum distribution [multiplication of (c) and (d)]. All distributions are normalized.

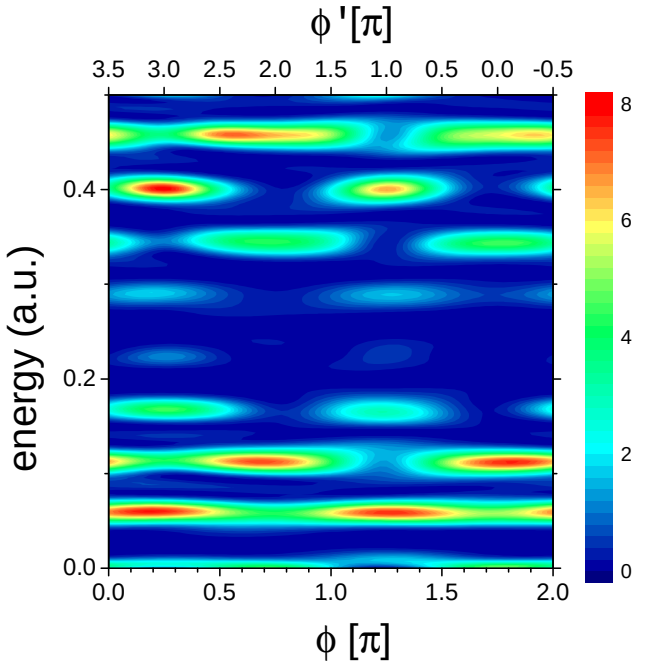

FIG. 14. Energy distribution in the forward direction as a function of the relative phase ϕ for the $\omega - 2\omega$ ionization within the SFA. In order to highlight the interference patterns we have multiplied the momentum distribution by $\exp(15E)$

We have also calculated the SFA forward emission spectrum as a function of the relative phase ϕ (see Fig. 14). In order to highlight the interference patterns we have multiplied the momentum distribution by $\exp(15E)$ to neutralize the exponential decay of the SFA as a function of the energy. One observe a very good agreement between SFA (Fig. 14) and SPA results (Figs. 13c and 13f). We think that the small deviations of the SFA from the SPA stem from the inclusion of the starting and ending ramps. It can be observed a ϕ-independent modulation with a minimum about 0.2 a.u. similar to the intrahalfcycle interference in Fig. 13d, 13e, and 13f. Besides,there is an anomaly in the alternation of ATIs and sidebands at energy close to the intrahalfcycle minimum at $E \sim 0.25$. This phenomenon could be due to the cooper minimum stemming from the $3p$ initial state of the argon atom.

Another important quantity to map out ionization phases in the $\omega - 2\omega$ protocol is the forward-backward $(\theta \leftrightarrow \pi - \theta)$ asymmetry of the photoelectron emission probability

$$A(E,\phi) = \frac{\frac{dP}{dE}(\theta = 0,\phi) - \frac{dP}{dE}(\theta = \pi,\phi)}{\frac{dP}{dE}(\theta = 0,\phi) + \frac{dP}{dE}(\theta = \pi,\phi)}, \qquad (29)$$

where the forward (backward) emission spectra $\frac{dP}{dE}(\theta = 0,\phi)$ ($\frac{dP}{dE}(\theta = \pi,\phi)$) are defined in Eq. (10). In Fig. 29a we show the SPA asymmetry parameter $A(E,\phi)$ as a function of the final electron kinetic energy E and the relative phase ϕ. The energy positions of ATIs are marked with a horizontal grey dash line whereas the position of sidebands are marked with a white dahline. In Fig. 29d we show the corresponding asymmetry parameter calculated within the SFA. At first shight, there are significant differences between the SPA and SFA results, however, when one inspect on the asymmetry at the position of the first ATI (in Fig. 29b) and second sideband (in Fig. 29c), similar oscillatory behaviors are found, maximizing the ATIs at $\phi = 0.25\pi$ and 1.25π and thee sidebands at $\phi = 0.75\pi$ and 1.75π.

For a close comparison between our SPA and SFA results with the perturbative theory developed in Ref. [45] accompanying an experiment for the ionization of atomic argon by a $\omega - 2\omega$ and also our recent perturbative theory developed in Ref. [46], we perform the transformation $t = t' + \phi'/(2\omega) - \pi/(4\omega)$ and $\phi = -\phi'/2 - \pi/4$ in Eq. (17), becoming the electric field in Eq. (30) equivalent

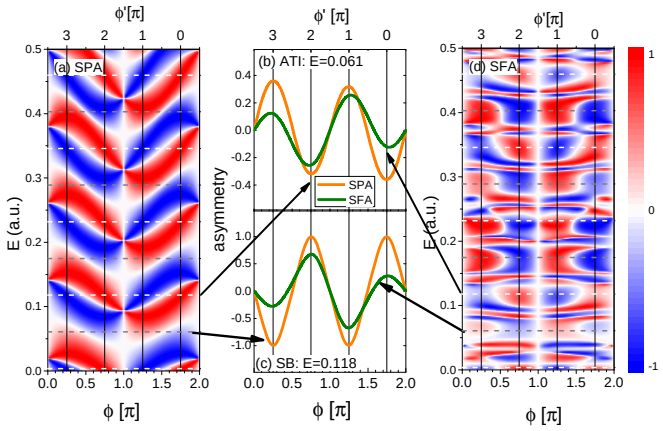

FIG. 15. Asymmetry parameter as a function of the energy E and relative phase ϕ in (a) for the SPA and (d) for the SFA. The horizontal dash lines indicate the energy positions of ATIs (grey) and sidebands (white). In (b) the asymmetry parameter for the first ATI (at $E = 0.061$) is plotted for the SPA and the SFA. In (d) the asymmetry parameter for the second sideband (at $E = 0.118$) is plotted for the SPA and the SFA.

to the following expression [see Eq. (1) of Ref. [45] only differing in a factor 2 for the definition of the frequencies, and Eq. (1) of Ref. [46],

$$\vec{F}(t') = f(t') \left[F_{2\omega} \sin\left(2\omega t' + \phi'\right) + F_{\omega} \sin(\omega t')\right] \hat{z}, \quad (30)$$

where we have supposed that the envelope $f(t)$ remains invariant due to its smoothness as a function of time. In Eq. (30) ϕ' is the relative phase of the second harmonic with respect to the fundamental laser field. Figs. 5, 13c, 13f, and 15 show that the ATIs maximize at $\phi_0 = \pi/4$ and $5\pi/4$, which is equivalent to $\phi_0' = -2\left(\phi_0 + \pi/4\right) = \pi$, and 3π, whereas the sidebands maximize at $\phi_0 = 3\pi/4$ and $7\pi/4$, which is equivalent to $\phi_0' = -2\left(\phi_0 + \pi/4\right) = 0$, and 2π (modulo 2π). Therefore, there are an agreement not only between our SFA and SPA calculations but also with our own perturbation theory [46] and the perturbation theory in Ref. [45].

III. CONCLUSIONS

We have developed a non-perturbative strong field theory for the atomic ionization by a linearly polarized $\omega - 2\omega$ laser pulse. We have derived the formation of sidebands as a result of the interplay between inter- and interhalfcycle interference patterns stemming from the effect of a ω field with respect to a stronger 2ω component. We have individualized both interhalf- and intrahalfcycle interferences conforming the intracycle interference pattern. We show that phase delays calculated within our SPA agree not only with our SFA calculations but also with previous perturbation theories [45, 46] extending their validity to stronger pulses.

ACKNOWLEDGEMENTS

This work was supported by CONICET PIP0386, PICT-2016-0296 PICT-2017-2945 and PICT-2016-3029 of ANPCyT (Argentina). D.G.A especially thanks S. Eckart, M. Dalhström, and M. Bertolino for fruitfull discussions.

[1] L V Keldysh. Ionization in the field of a strong electromagnetic wave. *Zh. Eksperim. i Teor. Fiz.*, 47, 11 1964.
[2] L V Keldysh. Ionization in the field of a strong electromagnetic wave. *Sov. Phys. JETP*, 20, 1965.
[3] B. Bergues, Z. Ansari, D. Hanstorp, and I. Y. Kiyan. Photodetachment in a strong laser field: An experimental test of Keldysh-like theories. *Phys. Rev. A*, 75(6):063415, June 2007.
[4] P. Agostini, F. Fabre, G. Mainfray, G. Petite, and N. K. Rahman. Free-Free Transitions Following Six-Photon Ionization of Xenon Atoms. *Physical Review Letters*, 42:1127–1130, April 1979.
[5] F. H. M. Faisal. Multiple absorption of laser photons by atoms. *Journal of Physics B Atomic Molecular Physics*, 6(4):L89–L92, April 1973.
[6] F. H. M. Faisal. Collision of electrons with laser photons in a background potential. *Journal of Physics B Atomic Molecular Physics*, 6(11):L312–L315, November 1973.
[7] P. B. Corkum, N. H. Burnett, and M. Y. Ivanov. Subfemtosecond pulses. *Opt. Lett.*, 19(22):1870–1872, Nov 1994.
[8] M. Lewenstein, K. C. Kulander, K. J. Schafer, and P. H. Bucksbaum. Rings in above-threshold ionization: A quasiclassical analysis. *Phys. Rev. A*, 51:1495–1507, Feb 1995.
[9] M. Ivanov, P. B. Corkum, T. Zuo, and A. Bandrauk. Routes to control of intense-field atomic polarizability. *Phys. Rev. Lett.*, 74:2933–2936, Apr 1995.
[10] S. Bivona, G. Bonanno, R. Burlon, D. Gurrera, and C. Leone. Signature of quantum interferences in above-threshold detachment of negative ions by a short infrared pulse. *Phys. Rev. A*, 77(5):051404, May 2008.
[11] Diego G. Arbó, Kenichi L. Ishikawa, Klaus Schiessl, Emil Persson, and Joachim Burgdörfer. Intracycle and intercycle interferences in above-threshold ionization: The time grating. *Phys. Rev. A*, 81:021403, Feb 2010.
[12] Diego G. Arbó, Kenichi L. Ishikawa, Klaus Schiessl, Emil Persson, and Joachim Burgdörfer. Diffraction at a time grating in above-threshold ionization: The influence of the coulomb potential. *Phys. Rev. A*, 82:043426, Oct 2010.
[13] D. G. Arbó, K. L. Ishikawa, E. Persson, and J. Burgdörfer. Doubly differential diffraction at a time grating in above-threshold ionization: Intracycle and intercycle interferences. *Nuclear Instruments and Methods in Physics Research B*, 279:24–30, May 2012.

[14] Xinhua Xie, Stefan Roither, Daniil Kartashov, Emil Persson, Diego G. Arbó, Li Zhang, Stefanie Gräfe, Markus S. Schöffler, Joachim Burgdörfer, Andrius Baltuška, and Markus Kitzler. Attosecond probe of valence-electron wave packets by subcycle sculpted laser fields. *Phys. Rev. Lett.*, 108:193004, May 2012.

[15] Diego G. Arbó, Stefan Nagele, Xiao-Min Tong, Xinhua Xie, Markus Kitzler, and Joachim Burgdörfer. Interference of electron wave packets in atomic ionization by subcycle sculpted laser pulses. *Phys. Rev. A*, 89:043414, Apr 2014.

[16] J. Itatani, F. Quéré, G. L. Yudin, M. Yu. Ivanov, F. Krausz, and P. B. Corkum. Attosecond streak camera. *Phys. Rev. Lett.*, 88:173903, Apr 2002.

[17] E. Goulielmakis, M. Uiberacker, R. Kienberger, A. Baltuska, V. Yakovlev, A. Scrinzi, Th. Westerwalbesloh, U. Kleineberg, U. Heinzmann, M. Drescher, and F. Krausz. Direct measurement of light waves. *Science*, 305(5688):1267–1269, 2004.

[18] E. Goulielmakis, V. S. Yakovlev, A. L. Cavalieri, M. Uiberacker, V. Pervak, A. Apolonski, R. Kienberger, U. Kleineberg, and F. Krausz. Attosecond control and measurement: Lightwave electronics. *Science*, 317(5839):769–775, 2007.

[19] V. Véniard, R. Taïeb, and A. Maquet. Two-Color Multiphoton Ionization of Atoms Using High-Order Harmonic Radiation. *Physical Review Letters*, 74:4161–4164, May 1995.

[20] Valérie Véniard, Richard Taïeb, and Alfred Maquet. Phase dependence of (n+1)-color (n ¿ 1) ir-uv photoionization of atoms with higher harmonics. *Phys. Rev. A*, 54:721–728, Jul 1996.

[21] P. M. Paul, E. S. Toma, P. Breger, G. Mullot, F. Augé, Ph. Balcou, H. G. Muller, and P. Agostini. Observation of a train of attosecond pulses from high harmonic generation. *Science*, 292(5522):1689–1692, 2001.

[22] M. Schultze, M. Fieß, N. Karpowicz, J. Gagnon, M. Korbman, M. Hofstetter, S. Neppl, A. L. Cavalieri, Y. Komninos, Th. Mercouris, C. A. Nicolaides, R. Pazourek, S. Nagele, J. Feist, J. Burgdörfer, A. M. Azzeer, R. Ernstorfer, R. Kienberger, U. Kleineberg, E. Goulielmakis, F. Krausz, and V. S. Yakovlev. Delay in Photoemission. *Science*, 328(5986):1658, June 2010.

[23] K. Klünder, J. M. Dahlström, M. Gisselbrecht, T. Fordell, M. Swoboda, D. Guénot, P. Johnsson, J. Caillat, J. Mauritsson, A. Maquet, R. Taïeb, and A. L'Huillier. Publisher's Note: Probing Single-Photon Ionization on the Attosecond Time Scale [Phys. Rev. Lett. 106, 143002 (2011)]. *Phys. Rev. Lett.*, 106(16):169904, April 2011.

[24] D. Guénot, K. Klünder, C. L. Arnold, D. Kroon, J. M. Dahlström, M. Miranda, T. Fordell, M. Gisselbrecht, P. Johnsson, J. Mauritsson, E. Lindroth, A. Maquet, R. Taïeb, A. L'Huillier, and A. S. Kheifets. Photoemission-time-delay measurements and calculations close to the 3s-ionization-cross-section minimum in Ar. *Phys. Rev. A*, 85(5):053424, May 2012.

[25] D. Guénot, D. Kroon, E. Balogh, E. W. Larsen, M. Kotur, M. Miranda, T. Fordell, P. Johnsson, J. Mauritsson, M. Gisselbrecht, K. Varjù, C. L. Arnold, T. Carette, A. S. Kheifets, E. Lindroth, A. L'Huillier, and J. M. Dahlström. Measurements of relative photoemission time delays in noble gas atoms. *Journal of Physics B Atomic Molecular Physics*, 47(24):245602, December 2014.

[26] Jaco Fuchs, Nicolas Douguet, Stefan Donsa, Fernando Martin, Joachim Burgdörfer, Luca Argenti, Laura Cattaneo, and Ursula Keller. Time delays from one-photon transitions in the continuum. *Optica*, 7(2):154, February 2020.

[27] J. M. Dahlström, D. Guénot, K. Klünder, M. Gisselbrecht, J. Mauritsson, A. L'Huillier, A. Maquet, and R. Taïeb. Theory of attosecond delays in laser-assisted photoionization. *Chemical Physics*, 414:53–64, March 2013.

[28] S. Nagele, R. Pazourek, J. Feist, and J. Burgdörfer. Time shifts in photoemission from a fully correlated two-electron model system. *Phys. Rev. A*, 85(3):033401, March 2012.

[29] Renate Pazourek, Johannes Feist, Stefan Nagele, and Joachim Burgdörfer. Attosecond Streaking of Correlated Two-Electron Transitions in Helium. *Phys. Rev. Lett.*, 108(16):163001, April 2012.

[30] A. S. Kheifets. Time delay in valence-shell photoionization of noble-gas atoms. *Phys. Rev. A*, 87(6):063404, June 2013.

[31] Johannes Feist, Oleg Zatsarinny, Stefan Nagele, Renate Pazourek, Joachim Burgdörfer, Xiaoxu Guan, Klaus Bartschat, and Barry I. Schneider. Time delays for attosecond streaking in photoionization of neon. *Phys. Rev. A*, 89(3):033417, March 2014.

[32] Jing Su, Hongcheng Ni, Andreas Becker, and Agnieszka Jaroń-Becker. Numerical simulation of time delays in light-induced ionization. *Phys. Rev. A*, 87(3):033420, March 2013.

[33] Renate Pazourek, Stefan Nagele, and Joachim Burgdörfer. Attosecond chronoscopy of photoemission. *Reviews of Modern Physics*, 87(3):765–802, July 2015.

[34] D. I. R. Boll and O. A. Fojón. Atomic RABBITT-like experiments framed as diatomic molecules. *Journal of Physics B Atomic Molecular Physics*, 49(18):185601, September 2016.

[35] D. W. Schumacher, F. Weihe, H. G. Muller, and P. H. Bucksbaum. Phase dependence of intense field ionization: A study using two colors. *Phys. Rev. Lett.*, 73(10):1344–1347, September 1994.

[36] D. G. Arbó, C. Lemell, S. Nagele, N. Camus, L. Fechner, A. Krupp, T. Pfeifer, S. D. López, R. Moshammer, and J. Burgdörfer. Ionization of argon by two-color laser pulses with coherent phase control. *Phys. Rev. A*, 92(2):023402, August 2015.

[37] Fritz Ehlotzky. Atomic phenomena in bichromatic laser fields. *Physics Reports*, 345(4):175–264, May 2001.

[38] H. G. Muller, P. H. Bucksbaum, D. W. Schumacher, and A. Zavriyev. Above-threshold ionisation with a two-colour laser field. *Journal of Physics B Atomic Molecular Physics*, 23(16):2761–2769, August 1990.

[39] M. R. Thompson, M. K. Thomas, P. F. Taday, J. H. Posthumus, A. J. Langley, L. J. Frasinski, and K. Codling. One and two-colour studies of the dissociative ionization and Coulomb explosion of H_2 with intense Ti:sapphire laser pulses. *Journal of Physics B Atomic Molecular Physics*, 30(24):5755–5772, December 1997.

[40] B. Sheehy, B. Walker, and L. F. Dimauro. Phase Control in the Two-Color Photodissociation of HD^+. *Phys. Rev. Lett.*, 74(24):4799–4802, June 1995.

[41] Hideki Ohmura, Taisuke Nakanaga, and M. Tachiya. Coherent Control of Photofragment Separation in the Disso-

ciative Ionization of IBr. *Phys. Rev. Lett.*, 92(11):113002, March 2004.

[42] M. Fifirig, A. Cionga, and F. Ehlotzky. Elliptic dichroism in hydrogen ionization by a coherent superposition of two harmonics. *European Physical Journal D*, 23(3):333–336, June 2003.

[43] Aurelia Cionga, Magda Fifirig, and Fritz Ehlotzky. Dichroic effects in the two-colour, two-photon ionization of hydrogen. *Journal of Modern Optics*, 50(3):615–620, March 2003.

[44] S. De, I. Znakovskaya, D. Ray, F. Anis, Nora G. Johnson, I. A. Bocharova, M. Magrakvelidze, B. D. Esry, C. L. Cocke, I. V. Litvinyuk, and M. F. Kling. Field-Free Orientation of CO Molecules by Femtosecond Two-Color Laser Fields. *Phys. Rev. Lett.*, 103(15):153002, October 2009.

[45] Lucas J. Zipp, Adi Natan, and Philip H. Bucksbaum. Probing electron delays in above-threshold ionization. *Optica*, 1(6):361, December 2014.

[46] S. D. López, S. Donsa, S. Nagele, D. G. Arbó, and J. Burgdörfer. Phase delays in $\omega - 2\omega$ above-threshold ionization. *arXiv e-prints*, page arXiv:2107.12414, July 2021.

[47] Mattias Bertolino and Jan Marcus Dahlström. Multiphoton interaction phase shifts in attosecond science. *Physical Review Research*, 3(1):013270, March 2021.

[48] P. A. Macri, J. E. Miraglia, and M. S. Gravielle. Ionization of hydrogen targets by short laser pulses. *Journal of the Optical Society of America B Optical Physics*, 20:1801–1806, September 2003.

[49] D. G. Arbó, J. E. Miraglia, M. S. Gravielle, K. Schiessl, E. Persson, and J. Burgdörfer. Coulomb-Volkov approximation for near-threshold ionization by short laser pulses. *Physical Review A*, 77(1):013401, January 2008.

[50] Maciej Lewenstein, Li You, J. Cooper, and K. Burnett. Quantum field theory of atoms interacting with photons: Foundations. *Phys. Rev. A*, 50(3):2207–2231, September 1994.

[51] D.M. Wolkow. Uber eine klasse von lösungen der diracschen gleichung. *Zeitschrift für Physik*, 94(3-4):250–260, 1935.

[52] R. Della Picca, A. A. Gramajo, S. D. López, and D. G. Arbó. XUV+IR photoionization of argon atoms: selection of sideband orders. *J. Phys. Conf. Series*, 2020. In press.

[53] Diego G. Arbó, Konstantinos I. Dimitriou, Emil Persson, and Joachim Burgdörfer. Sub-poissonian angular momentum distribution near threshold in atomic ionization by short laser pulses. *Phys. Rev. A*, 78:013406, Jul 2008.

[54] A. A. Gramajo, R. Della Picca, and D. G. Arbó. Electron emission perpendicular to the polarization direction in laser-assisted XUV atomic ionization. *Phys. Rev. A*, 96(2):023414, August 2017.

[55] A. A. Gramajo, R. Della Picca, S. D. López, and D. G. Arbó. Intra- and intercycle interference of angle-resolved electron emission in laser-assisted XUV atomic ionization. *Journal of Physics B Atomic Molecular Physics*, 51(5):055603, March 2018.

[56] P. A. Macri, J. E. Miraglia, M. S. Grabielle, F. D. Colavecchia, C. R. Garibotti, and G. Gasaneo. Theory with correlations for ionization in ion-atom collisions. *Physical Review A*, 57:2223–2226, March 1998.

[57] A K Kazansky and N M Kabachnik. Calculations of the double differential cross section for attosecond laser-assisted photoionization of atoms. *Journal of Physics B: Atomic, Molecular and Optical Physics*, 39(24):5173, 2006.

[58] D. Belkić, R. Gayet, and A. Salin. Electron capture in high-energy ion-atom collisions. *Physics Report*, 56:279–369, December 1979.